Real-Space Charge Density Profiling of Electrode-Electrolyte Interfaces with Angstrom Depth-Resolution

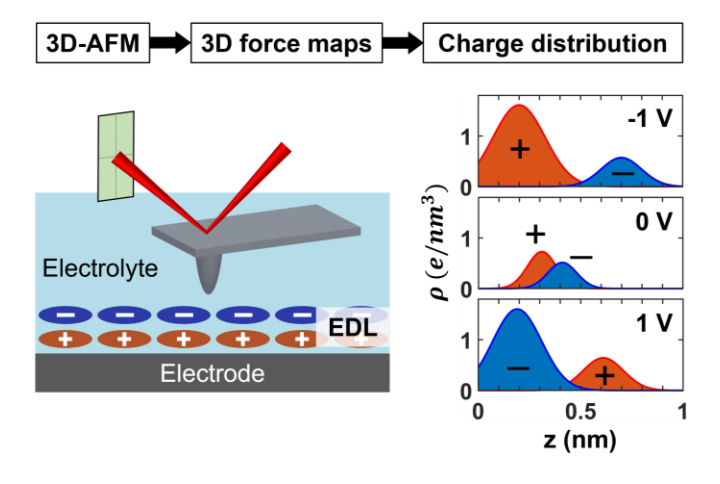
Lalith Krishna Samanth Bonagiri^{1,2}, Kaustubh S. Panse^{1,3}, Shan Zhou^{1,3}, Haiyi Wu⁴, Narayana R. Aluru⁴, and Yingjie Zhang^{1,3}*

- 1. Materials Research Laboratory, University of Illinois, Urbana, IL 61801, USA
- 2. Department of Mechanical Science and Engineering, University of Illinois, Urbana, IL 61801, USA
- 3. Department of Materials Science and Engineering, University of Illinois, Urbana, IL 61801, USA
- 4. Walker Department of Mechanical Engineering and Oden Institute for Computational Engineering & Sciences, The University of Texas at Austin, Austin, TX 78712, USA

Abstract: The accumulation and depletion of charges at electrode-electrolyte interfaces is crucial for all types of electrochemical processes. However, the spatial profile of such interfacial charges remains largely elusive. Here we develop charge profiling 3D atomic force microscopy (CP-3D-AFM) to experimentally quantify the real-space charge distribution of the electrode surface and electric double layers (EDLs) with angstrom depth-resolution. We first measure the 3D force maps at different electrode potentials using our recently developed electrochemical 3D-AFM. Through statistical analysis, peak deconvolution and electrostatic calculations, we derive the depth profile of the local charge density. We perform such charge profiling for two types of emergent electrolytes, ionic liquids and highly concentrated aqueous solutions, observe pronounced subnanometer charge variations, and find the integrated charge densities to agree with those derived from macroscopic electrochemical measurements.

Keywords: Electrode-electrolyte interface, electric double layer, electrochemical atomic force microscopy, 3D atomic force microscopy, double layer charging, charging profiling, atomic resolution imaging

TOC graphic:



^{*}Correspondence to: yjz@illinois.edu

Introduction

The core of electrochemistry is the interconversion between electrical and chemical energy at the electrode-electrolyte interface. Such conversion processes inevitably require the local accumulation and depletion of charges at the interface, including the electrode surface and the solvation layers, or EDLs. The spatial charge distribution, therefore, is a key descriptor of the microscopic mechanisms of all types of electrochemical processes. Examples are: 1) in supercapacitors, the charge density distribution of EDLs is directly responsible for capacitive energy storage; ¹ 2) in lithium-ion batteries, the accumulation of solvated Li⁺ ions on the surface of the negative electrode is essential for the electrode passivation (formation of solid-electrolyte interphases, or SEIs) and Li⁺ intercalation processes, which in turn determines the energy density and battery stability;^{2–5} 3) in electrocatalytic processes (for fuel cells, batteries, etc.), the catalytic activities are strongly modulated by the heterogeneous charge arrangements of the local electrode surface and the various ionic species in the EDL. 6-10 Despite their key role in electrochemistry, the interfacial charge density profiles have remained a long-standing puzzle. While classical theories such as the Gouy-Chapman-Stern model can predict the overall electrostatic profiles, the inner, discrete EDLs within ~1 nanometer from the electrode surface remain elusive, even though they are oftentimes the most crucial in regulating electrochemical processes. This is because classical electrostatics by itself cannot predict the discreteness of the molecular layers in the inner EDLs, while experimentally these subnanometer-thick regions pose significant challenges for in-situ characterization due to the small size scale, volatility and mobile nature of the liquid electrolyte, as well as the buried nature of these interfaces.

A host of techniques have been used to characterize the EDL structure, each having its own limitations. Spectroscopy methods, such as X-ray absorption, Fourier-transform infrared, sum frequency generation, and Raman spectroscopies, have provided information on the chemical bonding states at electrode-electrolyte interfaces, but lack spatial resolution. 11-14 Microscopy tools. including (scanning) transmission electron microscopy and scanning tunneling microscopy, have been able to resolve individual atoms of solid materials and surfaces, but are not sensitive to the mobile liquid species in the EDL. 15,16 X-ray diffraction has also been used, which allows the determination of the average distance between the first EDL and the electrode surface, although the charge density profile, in-plane packing structure and upper layers cannot be determined. 17,18 In the past decade, significant advancements have been made in liquid-phase AFM, which has enabled the detection of the vertical layer separations and even the 3D density maps of EDLs via sensitive force measurements. 19-33 Our recent work has demonstrated an electrochemical 3D-AFM (EC-3D-AFM) technique that has further achieved atomic resolution 3D imaging of EDLs in working electrochemical cells.^{34,35} The 3D force maps obtained from EC-3D-AFM can be approximated as the molecular density distribution, which is a result of the time-averaged thermal motion of molecules in the EDL. However, since the molecular density has contribution from multiple types of molecular/ionic species, it remains challenging to deconvolute each species and quantify the spatial charge distribution profile.

In addition to structural characterization, efforts have also been made to determine the spatial electrostatic potential profiles of electrode-electrolyte interfaces. Kelvin probe force microscopy

(KPFM), a method widely used for imaging the surface potential of solids in air and in vacuum, has been employed to map the in-plane potential distribution of the electrode surface immersed in liquid electrolytes.³⁶ On the other hand, to achieve depth profiling of the potential, ambient pressure X-ray photoelectron spectroscopy (APXPS) was employed, and the potential drop across EDL was indirectly extracted from the width of the core-level photoelectron peaks.³⁷ In recent years, another scanning probe-based method, open-loop electric potential microscopy (OL-EPM), is being actively developed to map the 3D potential distribution of electrode-electrolyte interfaces via quantitative electrostatic force measurements.^{38–40} However, due to the charge screening effects in KPFM and OL-EPM and the limited depth resolution (~10 nm) of APXPS, all of these techniques are limited to highly diluted solutions (no more than ~10 mM) that are far from realistic electrochemical conditions. Note that, even in such dilute electrolytes, while the EDL is mostly diffuse with overall width higher than a few nanometers, the inner Helmholtz plane (within a few angstroms from the electrode surface) may still have a significant or dominant contribution to the overall charge and potential profiles. However, such inner EDLs are hidden from existing potential mapping measurements.

Here we take a major step towards angstrom-scale 3D charge density profiling at electrode-electrolyte interfaces. Considering that EC-3D-AFM provides molecular density profiles yet with no chemical/charge sensitivity, while electrostatic models offer solutions of charge density distribution given the input of the discrete molecular positions, we combine EC-3D-AFM and electrostatic calculations synergistically to obtain the spatial charge distribution. The developed method, named CP-3D-AFM, enables quantitative charge density profiling of both the local electrode surface and EDLs with angstrom depth-resolution.

Results and Discussion

Protocols for charge profiling of electrode-electrolyte interfaces. The overall measurement and analysis process for CP-3D-AFM is shown in Figure 1. We first perform DC mode 3D force mapping of the electrode-electrolyte interface at a series of different electrode potentials, where the force is recorded as the probe moves sinusoidally along the z direction (10-100 Hz) as well as linearly along the x, y directions (<1 Hz) (Figure 1a). We then extract and plot the count distribution (number of points at each small z-interval in the force-distance curve) of x-z crosssection frames (Figure 1b). Note that these counts roughly represent the retention time of the AFM probe at each EDL layer when pushing down and eventually penetrating through the layer. Higher molecular density will result in longer tip retention time as the cantilever moves down. Therefore, the count number can approximately represent the relative molecular density at each spatial location. The validity of this approximation is verified by the agreement between our experimental results and molecular dynamics (MD) simulations on ionic liquids,³⁴ as well as the consistency with other reported results on EDL molecular density analysis. ²⁵ In particular, for the system of an ionic liquid, 1-ethyl-3-methylimidazolium bis(trifluoromethylsulfonyl)imide (EMIM-TFSI) on highly oriented pyrolytic graphite (HOPG), our 3D-AFM results reveal force spikes with 0.4-0.5nm separation in the EDL, which agrees with the expected nearest neighbor distance between EMIM⁺ and TFSI⁻, thus confirming that both cations and anions contribute to the 3D-AFM

signal.^{25,34,41} Since the electrode is atomically flat, the molecular density variation in the EDL is much more pronounced along the z direction compared to the in-plane x, y directions. Therefore, we focus mainly on the z-dependence of the count maps, although our method can be easily extended to analyze the in-plane charge variations of heterogeneous electrodes and EDLs. To maximize the signal-to-noise ratio along z, we integrate along the x direction and obtain the count histogram as a function of z (Figure 1c). More detailed description of the 3D-AFM measurement process and analysis of the count maps and histograms is presented in our previous publication.³⁴

In general, the count / molecular density maps from 3D-AFM contain contributions from all the species in the electrolyte, which may include neutral non-polar molecules, neutral polar molecules, and charged molecules/ions. An accurate charge profiling will require all the species to be taken into account for peak deconvolution. However, for many highly ionic electrolytes, such as ionic liquids and highly concentrated solutions (salt concentration of a few molar), neutral species are either absent/negligible or expected to form molecular complexes together with charged ions. ^{22,42,43} In these systems, unless multiple positively (or negatively) charged species exist in the same electrolyte, it is oftentimes sufficient to use two charged species components, one positive and the other negative, to deconvolute the overall molecular density peaks.

As we change the electrode potential, these charged species are expected to move along the z direction as a result of the electrostatic interaction with the electrode. Therefore, we use the following protocols to deconvolute the count histogram to charge density peaks: 1) subtract a double exponential background which is due to the nonlinear motion of the cantilever during tip approach; 2) for each count peak, assume it consists of only positive charges, only negative charges, or a combination of both, and perform a Gaussian peak fit for each species assumed to be present; 3) as electrode potential becomes more positive, we assume that positive charges move farther away from the electrode surface, while negative charges move closer to the surface; 4) only the first sets of positively and negatively charged peaks are analyzed, which are assumed to have the dominant contribution to the EDL capacitance, as shown in our previous work³⁴ and further analysis (Supporting Information, Figure S1). Under these assumptions, the count histograms can be deconvoluted into individual charged peaks, as shown in Figure 1d.

The charge density peaks obtained from the count histograms reveal the relative charge distribution along the z direction, but are in arbitrary units and do not directly provide the quantitative density values at any given position. In order to quantify the charge density profile, we take advantage of the known electrode potential, and use the Poisson's equation $\nabla^2 \phi = -\frac{\rho}{\epsilon}$ (ϕ : potential, ρ : charge density, ϵ : dielectric constant) to rescale and quantify ρ as a function of z in the EDL (Figure 1e). Note that the electrode potential vs the bulk liquid potential, a key parameter for electrostatic calculations, is typically different from the experimentally applied electrode voltage (vs Pt quasi-reference electrode) with a constant offset. However, the change of electrode potential ($\Delta \phi_s$) is independent of the reference. Therefore, we use the convergence of $\Delta \phi_s$ as the key criteria to evaluate and reiterate the peak deconvolution process, and to rescale the eventual charge density values. After the EDL charge density profiles are finalized, we take advantage of the overall charge neutrality condition of the electrode-electrolyte interface to obtain the electrode surface charge density (σ_s), by integrating ρ over z throughout the whole EDL and then reversing the sign. An

example of the calculated quantitative charge density distributions of both the electrode surface and EDL is shown in Figure 1f.

The detailed peak deconvolution and electrostatic calculation processes are elaborated in Note S1.

Charge density profiling of ionic liquid / electrode interfaces. We use HOPG electrode, which is a model system that represents the typical carbon-based electrodes used in batteries and supercapacitors. As to the electrolyte, we first choose EMIM-TFSI, which has low volatility and a large electrochemical stability window, and is being widely explored for electrocatalysis and energy storage applications. 44,45 Our previous work has demonstrated EC-3D-AFM imaging of this ionic liquid, and revealed multiple discrete molecular density peaks in the EDL.³⁴ Within the potential range of -1 to 1 V (vs Pt), we observed atomically-clean electrodes, as well as pronounced potential-dependent changes in the x-z count maps, although the actual charge distribution has been puzzling. To solve this problem, we apply the CP-3D-AFM method as specified in Figure 1. For the EMIM-TFSI / HOPG system, the detailed electrostatic deconvolution procedures and parameters are listed in Figure S2 and Table S1. The obtained results on quantitative charge density profiles and electrostatic potential distribution are shown in Figure 2. As a result of our established electrostatic protocols, the assigned anion and cation peaks move in opposite directions as the potential changes, the former closer to the electrode while the latter farther away at more positive potentials. The cation and anion peaks have large overlap at small potentials $(0, \pm 0.5 \text{ V})$ and nearly completely split apart at high potentials (±1 V) (Figure 2a), which agrees with our previous MD simulation results.³⁴

From the CP-3D-AFM method, we obtain electrode surface charge densities of -0.35, -0.17, -0.04, 0.04, and 0.30 e/nm² at -1, -0.5, 0, 0.5, and 1 V (vs Pt), respectively (Figure 2a). This result reveals a strong capacitive charging effect, as expected from the pronounced changes in the position of the EDL charge peaks at different electrode potentials. It also shows that the potential of zero charge (PZC) is between 0 and 0.5 V. To further evaluate the EDL charging mechanism, we integrate the charge peak closest to the electrode surface at each potential (the positive peak at zero and negative potentials, and negative peak at positive potentials) to obtain its overall areal charge density. The results are 0.48, 0.30, 0.13, -0.10, -0.45 e/nm² at -1, -0.5, 0, 0.5 and 1 V, respectively. The ratio of these areal charge densities to the corresponding electrode surface charge densities (in absolute values) are 1.4, 1.8, 3.3, 2.5, and 1.5, respectively. Therefore, the first charged layer in the EDL overbalances the electrode's surface charge, which concurs with the "overscreening" effect proposed by Kornyshev et al. in a continuum theory of ionic liquids. 46 This likely results from the strong Coulomb interaction between cations and anions. Kornyshev et al. also predicted a transition from overscreening to "crowding" effects as the electrode potential increases from 0.26 V to 2.6 V (away from PZC), since significant amounts of charges at the electrode surface can induce strong electrostatic interactions that overcome the intermolecular correlations of the EDL. Our results show a similar trend where overscreening becomes weaker as the electrode potential moves farther away from PZC (in either the positive or negative direction). While we do not observe crowding effects within our experimental potential range, this does not preclude the possibility of crowding at much higher potentials.

We further calculate the electrostatic potential profile along the z direction, with results shown in Figure 2b. In all the calculated results, the potential of the bulk electrolyte is taken as 0 V. At the experimental electrode potential of 0 V vs Pt, we obtain $\phi_s = -0.17 V$, which is similar to the ϕ_s at the PZC in our previous MD simulation.³⁴ Throughout the full measured potential range, as the experimental potential changes by 0.5 V, the calculated ϕ_s changes by the same amount. In all the electrostatic potential profiles, the potential first becomes more positive or negative as z become smaller, and then reverses the direction of the change within a few angstroms away from the electrode surface. These potential profiles are in sharp contrast to the smooth, unidirectional potential changes predicted by the Gouy-Chapman-Stern model and observed in a previous study on highly diluted electrolyte solutions.³⁷ The observed abrupt turn of potential in the inner EDL is a result of the overscreening effect, i.e., the significant amounts of charge alteration within subnanometer distance.

Note that, in all of our results, z=0 nm corresponds to the lowest z position of the AFM probe. From an electrostatic perspective, however, the electrode potential and surface charge density should correspond to those at the center of the top-most graphene layer of the HOPG electrode, as shown in our previous MD simulations as well as other groups' results.^{34,47,48} Considering that the inter-layer spacing in graphite is ~0.34 nm, we take half of this distance, 0.17 nm, as the approximate separation between the end of the AFM tip and the center of the top-most carbon atoms of the HOPG electrode. Therefore, ϕ_s and σ_s are both obtained at z = -0.17 nm.

In order to verify the extracted EDL charge density profiles, it is desirable to directly compare the results with those from standard electrochemical measurements. To this end, we perform electrochemical impedance spectroscopy (EIS) of the EMIM-TFSI / HOPG system using the same electrochemical cell as that in EC-3D-AFM, except that no AFM probe is present. The raw EIS data plotted in the complex capacitance plane and the detailed equivalent circuit analysis are shown in Figure S3a and Note S2. The differential capacitance vs electrode potential obtained from EIS is plotted in Figure 3a. The capacitance values are in the same range with those from existing EIS studies of EMIM-TFSI. 49-51 These previous work reported different shapes of the capacitance-potential curve, including bell, camel, and "V" shapes, possibly due to the structural variations of the glassy carbon electrodes they used. 52 Our result on the well-defined HOPG electrode reveals "V" shape, i.e., the capacitance is minimum at PZC, and increases gradually as the potential becomes more positive or negative. This is likely because the overscreening effect becomes weaker as the potential deviates more from PZC, resulting in a larger EDL capacitance.

By integrating the differential capacitance (extracted from EIS) over electrode potential, we obtain the overall electrode charge density at different potentials, as shown in Figure 3b. We also plot the σ_s obtained from CP-3D-AFM, where each point represents the average value and standard deviation extracted from multiple x-z count maps at each potential (details shown in Figure S4). Note that the PZC values (vs Pt) obtained from EIS and CP-3D-AFM results show a small difference, likely due to the random potential fluctuations of the Pt quasi-reference electrode. Nevertheless, by applying a potential offset to the PZC, we can see that the charge density values obtained from these two methods are very close to each other. This is a strong proof of the validity of our CP-3D-AFM method.

Now that the CP-3D-AFM results are verified, we further compare them in detail with MD simulations for the EMIM-TFSI / HOPG system. In our prior work, ³⁴ we already obtained ϕ_s = PZC, PZC + 0.93 V, and PZC - 0.90 V at $\sigma_s = 0$, 0.28 e/nm², and -0.28 e/nm², respectively. As shown in Figure 3b, these data are highly consistent with both the EIS and CP-3D-AFM results. We have now performed further MD simulations at $\sigma_s = 0$, ± 0.24 e/nm², and ± 0.45 e/nm². In addition to the σ_s vs ϕ_s results that are again in agreement with our experimental data (Figure 3b), we have further compared the spatial distribution of charge and electrostatic potential in the EDL between MD and CP-3D-AFM results, as shown in Figures S5 and S6. We can see that the overall trends of these spatial profiles are consistent between these two types of data. While there are differences in the exact positions and/or values, this is as expected, due to two reasons: 1) although we have used highly reliable force fields (all-atom optimized potential for liquid simulations, or OPLS-AA) for MD simulation, 53,54 the simulation results likely still have some deviation from realistic systems since these classical force fields cannot capture all the atomistic interactions among the liquid molecules and between the liquid and solid; 2) while CP-3D-AFM is based on realistic experimental systems, its resolution is worse than that of MD, resulting in "smoothened" spatial profiles. Therefore, while both CP-3D-AFM and MD have room for further improvements, they are complementary to each other and can be jointly used for quantifying solid-liquid interfaces.

Charge density profiling of water-in-salt electrolyte / electrode interfaces. To demonstrate the general applicability of the CP-3D-AFM method, we perform charge density profiling of another type of emergent electrolyte, water-in-salt (WiS) system, which is composed of highly concentrated salt (> 5 m) in aqueous solution. Since its introduction in 2015, WiS electrolytes have been widely explored to make batteries with enhanced safety and reduced environmental impacts. In these systems, since the salt outnumbers the solvent, most of the water molecules are expected to be bound to the cations (typically alkali cations), although the exact cation solvation structure and EDL charge distribution are still largely unknown and under debate. A2,55,60-62 We choose 21 m LiTFSI in water electrolyte, which is the most widely studied WiS system. Since the amount of free water is likely much less than that of the bound water in this system, we use the two-component (i.e., [Li(H₂O)_x]⁺ and TFSI⁻) analysis to perform CP-3D-AFM.

Based on the cyclic voltammetry (CV) measurements (Figure S7), lattice-resolution imaging of the electrode surface (Figure 4a), and stability of the force-distance curves, we choose a potential window of -1-0.5 V to perform CP-3D-AFM for the WiS electrolyte / HOPG interface, which ensures reproducible EDL structure. Note that sporadic nanoclusters, likely due to redox processes of impurities, can form on the electrode surface and may strongly perturb the local EDL structure. Therefore, it is critical to verify the atomic-scale cleanliness of the local electrode area at each potential before performing EDL mapping at the same location. Our EC-3D-AFM setup, with atomic-scale resolution, is highly suitable for this purpose. Our x-y images of the HOPG surface (Figure 4a) reveal clear hexagonal lattice with lattice constant of \sim 0.25 nm, as expected for the HOPG basal plane structure. Right above the imaged HOPG lattice region, we obtain x-z count maps inside the EDL (Figure 4b). We observe multiple discrete EDL layers similar to the typical structures we detect for ionic liquids. The count vs z histograms, shown in Figure 4c, further reveal the trend of the layer position vs electrode potential. While fluctuations occur, the interlayer distance is typically \sim 4 Å among all the layers within the measured z range of 0-2 nm, smaller

than the \sim 5 Å spacing we observe for EMIM-TFSI (Figure S8). This is likely because either the $[\text{Li}(\text{H}_2\text{O})_x]^+$ complex (in WiS) is slightly smaller than the EMIM⁺ molecule (in EMIM-TFSI), or the former is more densely packed together with TFSI⁻ due to steric or other interaction effects. Note that the size of an EMIM⁺ molecule is around $0.9 \times 0.5 \times 0.3 \text{ nm}^3$, $^{63-65}$ while that of $[\text{Li}(\text{H}_2\text{O})_x]^+$ is likely in the range of 0.3-0.7 nm depending on the coordination number (taking into account of the simulated Li-O distance of \sim 0.2 nm and water diameter of \sim 0.3 nm). 42,66,67

We have performed 3D-AFM imaging of the WiS / HOPG system using multiple AFM probes, and find the resulting count histograms to be quite similar (examples shown in Figure S9). Such consistency is a prerequisite for reliable CP-3D-AFM analysis.

To carry out CP-3D-AFM analysis of the WiS electrolyte, we again assume that the first pair of charged layers have dominant contribution to the EDL charging behavior. We perform peak deconvolution under electrostatic constraints and quantify the inner-layer charge distribution, with detailed procedures and parameters specified in Figure S10 and Table S2. The final charge and potential profiles are shown in Figure 5. From the evolution of the electrode charge density, we find that the PZC is between -0.5 – 0 V. Compared to EMIM-TFSI, we observe similar potential dependent charge reconfiguration effects, as well as the overturn of the electrostatic potential profile within the EDL at each electrode potential. We also find that, when the electrode potential is near PZC, both positive and negative charge peaks are closer to the electrode surface in WiS (compared to EMIM-TFSI). This is likely due to the weaker intermolecular interaction and steric hindrance effects between [Li(H₂O)_x]⁺ and TFSI⁻ as they pack together in the first EDL, in contrast to the strongly interacting EMIM-TFSI ion pairs which may have larger hindrance effects. Such differences in intermolecular interaction effects have been observed in our recent work on Raman spectroscopy of bulk electrolytes and their EDLs.⁶⁸

Following the same process for evaluating the overscreening effects in EMIM-TFSI, we integrate the volumetric charge density profile of the peak closest to the electrode surface at each potential, obtain the areal charge density of this first charge layer, and calculate its ratio (in absolute value) to the corresponding electrode surface charge density. These "overscreening ratios" are found to be 1.3, 2.2, 2.1, 1.4 at -1 V, -0.5 V, 0 V and 0.5 V, respectively. Therefore, we conclude that overscreening effect also occurs in the WiS electrolyte, is strongest near PZC, and becomes weaker as potential deviates from PZC in both directions. Compared to EMIM-TFSI, we find overall smaller overscreening ratios, indicating weaker overscreening effect. This again reveals that the intermolecular interaction/correlation in WiS is likely weaker than that in EMIM-TFSI.

We further perform EIS measurements of the WiS electrolyte (Figure S3b). Via thorough equivalent circuit analysis (Note S2), we obtain the differential capacitance as a function of electrode potential (Figure 6a). Comparing the capacitance values at positive vs negative potentials (vs PZC), we observe a clear asymmetry – higher capacitance occurs at the positive side. This is in sharp contrast to the EIS results of EMIM-TFSI, where the negative side has larger differential capacitance. However, at the positive side, we find that the differential capacitance values are very similar between the WiS and EMIM-TFSI systems (Figure S11). This is likely because that, for both systems at potentials more positive than PZC, TFSI accumulates at the electrode surface and gradually becomes the dominant contributor to the EDL charge density, as shown in Figure 2a and

Figure 5b. Since TFSI⁻ has the same molecular structure in these two electrolytes, the capacitance values are also similar as observed, and the small offsets are likely due to the different intermolecular interaction effects. As to the positively charged species, EMIM⁺ has quasi-planar structure while $[Li(H_2O)_x]^+$ may have an overall nearly spherical shape (or other shape with a high degree of isotropy). As a result, the former may have an extra degree of freedom that contributes to EDL charging – the molecular orientation. According to our previous MD simulations, ³⁴ EMIM⁺ changes from tilted to flat orientation as the potential becomes more negative. Such orientation changes, in addition to the shift of the center of mass, can result in a pronounced decrease of the charge center – electrode surface distance and thus a large increase in capacitance. In contrast, the charge in the "bulky" $[Li(H_2O)_x]^+$ likely always resides at the center of this complex and thus its motion towards the electrode surface at negative potentials is more limited. As a result, the capacitance increase is smaller compared to that of EMIM-TFSI in the negative direction.

By integrating the differential capacitance from EIS results of WiS, we obtain charge density as a function of electrode potential, and plot the data together with those obtained from CP-3D-AFM (Figure 6b). Note that each CP-3D-AFM data point corresponds to the average of a series of x-z count maps / z histograms, as shown in Figure S12. We again observe strong agreement between results from the two different measurements, which confirms the validity and general applicability of our CP-3D-AFM method.

Conclusion

We have demonstrated a comprehensive method, CP-3D-AFM, to profile the charge density distribution of electrode-electrolyte interfaces with angstrom depth-resolution. Using this method, we have determined the real-space charge rearrangements of the ionic liquid / HOPG and WiS / HOPG interfaces, including the electrode surface and the EDLs. We observe overscreening effects in the EDL of both electrolytes, and found different asymmetric capacitive responses in the two systems likely due to differences in the size, shape, and composition of the positively charged species and their interaction with the anions.

While the electrolytes studied here can both be treated as binary systems for the purpose of charge deconvolution, our CP-3D-AFM method can be extended to systems containing multiple charged and neutral species. For these more complex electrolytes, we will need to deconvolute multiple peaks corresponding to different charged or neutral species, within a set of electrostatic constraints. Machine learning will also facilitate such deconvolution processes. Considering that most realistic electrochemical systems have charge concentration of at least 0.1 M or higher, their inner discrete EDLs play significant or dominant roles in capacitive charging and various redox activities.⁶⁹ We expect our CP-3D-AFM method to be capable of profiling the charge density of most of these inner EDLs. Therefore, this method will be broadly applicable to a large range of practical electrochemical devices including batteries, fuel cells, electrolyzers, and supercapacitors, and offer key molecular insights into their functioning mechanisms.

Methods

Sample and tip preparation. All the experiments were carried out using HOPG (Bruker) as working electrode. EMIM-TFSI was purchased from two sources, Thermo Fisher Scientific (>98%) and Iolitec (>99.9%), and no apparent differences were observed in the EC-3D-AFM results. LiTFSI salt (99.95%) was obtained from Sigma-Aldrich. EMIM-TFSI was vacuum annealed for ~24 hours at 105 °C and subsequently stored in an argon-filled glovebox. LiTFSI was stored aspurchased in a nitrogen-filled glovebox. To prepare the water-in-salt electrolyte, we added Milli-Q water (dispensed from MilliporeSigma water purification system) to LiTFSI salt, to reach a concentration of 21 m (molal), and then sonicated for ~3–5 minutes to ensure uniform mixing. FS-1500AuD AFM probes were purchased from Asylum Research. Prior to the day of measurement, thermal and cantilever tune of the AFM probe in air was captured. The probe was then cleaned by soaking in acetone for ~30 minutes, in IPA overnight, and in Milli-Q water for ~2 hours. Afterwards, the AFM probe was UV-Ozone cleaned (using UV/Ozone ProCleaner Plus from BioForce Nanosciences) for 5 minutes to remove any remaining organic contaminants, and then immediately mounted to the probe holder for EC-3D-AFM measurements. Detailed description of the AFM electrochemical cell is provided in our previous paper.³⁴ The cell parts were cleaned with acetone and/or IPA thoroughly. In the case of water-in-salt electrolyte, the cell parts were further cleaned with Milli-Q water. After the cell was assembled, we used scotch tape to peel off the surface layers of HOPG right before adding the electrolyte.

CV and EIS measurements. EIS with EMIM-TFSI as electrolyte was performed using the AFM electrochemical cell in the argon-filled glovebox (H₂O and O₂ levels were both < 0.1 ppm). A CHI660D electrochemical workstation was used, which was connected to the glovebox using a multi-pin feedthrough (obtained from Kurt J. Lesker). Co-axial cables were used for this connection to minimize noise. In the case of WiS electrolyte, CV and EIS were performed in the AFM electrochemical cell in ambient lab atmosphere. A Biologic SP-300 potentiostat was used for these measurements. For both electrolytes, HOPG was used as working electrode, and Pt ring/wire was used as reference and counter electrodes. For both electrolytes, EIS was measured at a series of electrode potentials; at each potential, the frequency was swept from 0.1 to 10⁶ Hz. In all the measurements using the AFM electrochemical cell, the surface area of the working electrode in contact with the electrolyte is ~0.636 cm² (a circular area with ~9 mm diameter).

EC-3D-AFM measurements. EC-3D-AFM measurements were carried out using an Asylum Cypher ES AFM as base system, with custom modifications. Detailed procedures are provided in our previous paper.³⁴

Data analysis. We used MATLAB to process both 3D-AFM and EIS data. Detailed procedures are provided in Notes S1 and S2.

MD simulations. MD simulations of EMIM-TFSI / HOPG were conducted using LAMMPS. The system setup, force field parameters and simulation methods are discussed in detail in our previous work.³⁵ After the system reached equilibrium, we extracted the charge density and center-of-mass (COM) profiles of the electrolyte. We then used Poisson's equation to calculate the electrode surface potential, based on the charge density profile of the EDL. These results are shown in Figure

3b. Considering that our CP-3D-AFM method extracts charge density based on the distribution of individual molecular species, to enable reliable comparison, we used similar approach to obtain charge density and electrostatic potential profiles of the EDL from MD simulations. Briefly, we assume that each EMIM⁺ / TFSI⁻ molecule contains a discrete charge at its COM, as an approximation; as a result, the COM profile of each species is the same as the corresponding charge number distribution, as shown in Figure S5. From the COM profiles, we further used Poisson's equation to calculate the electrostatic potential profiles, with results shown in Figure S6.

Figures

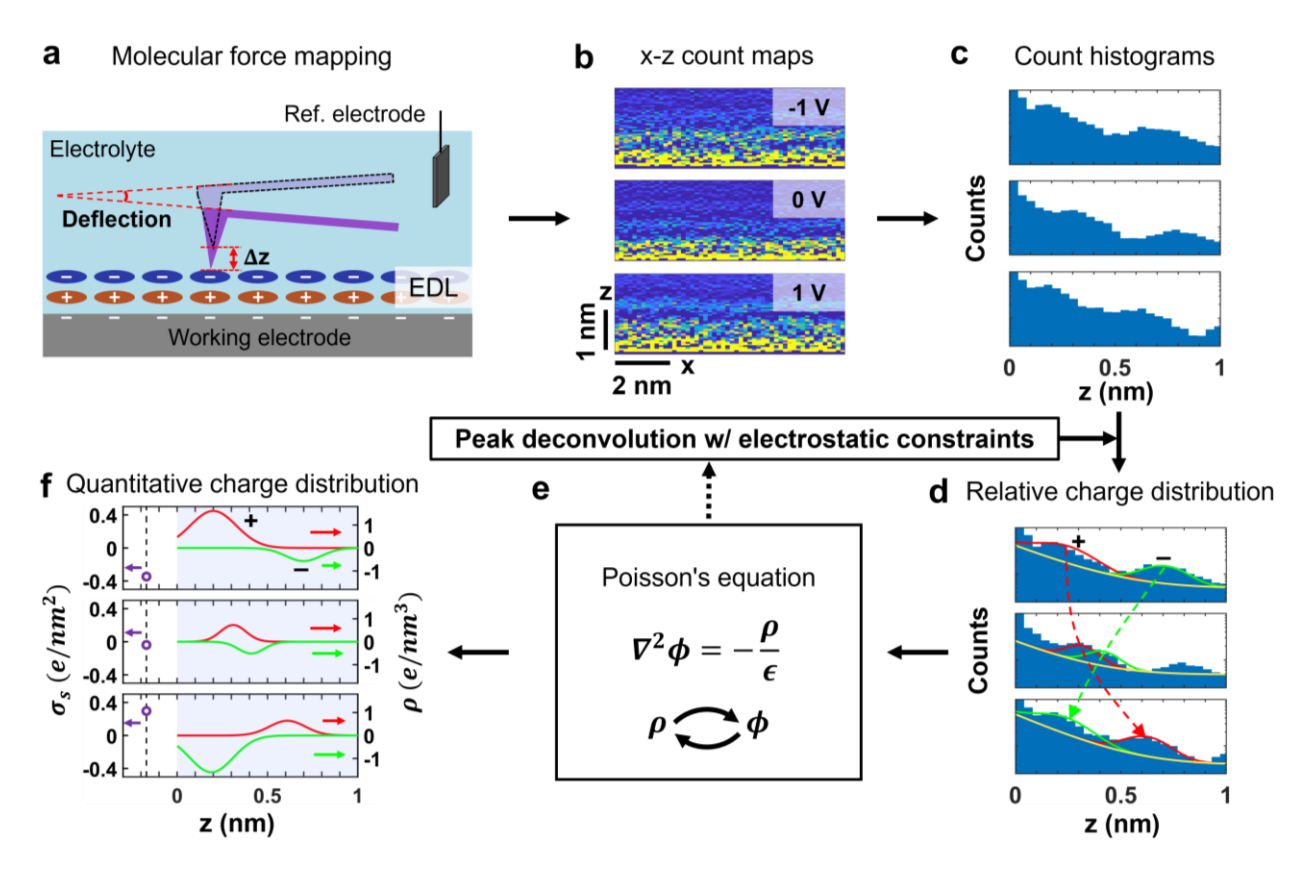


Figure 1. Summary of the CP-3D-AFM method. (a) Schematic depicting the EC-3D-AFM measurement process, where deflection (force) increases as the AFM probe reaches each layer of the EDL. (b) x-z count maps at different electrode potentials processed from the EC-3D-AFM data (plotted after background subtraction; detailed methods discussed in our previous work³⁴). (c) Count histograms vs z obtained from the corresponding x-z count maps. (d) Fitting of the charge distribution peaks. (e) Quantitative calculation of the spatial charge density and potential profiles via Poisson's equation through a reiterative peak deconvolution process. (f) Examples of the final calculated charge density profiles, including the volumetric charge density in the EDLs (ρ) as a function of z and the electrode surface charge density (σ_s).

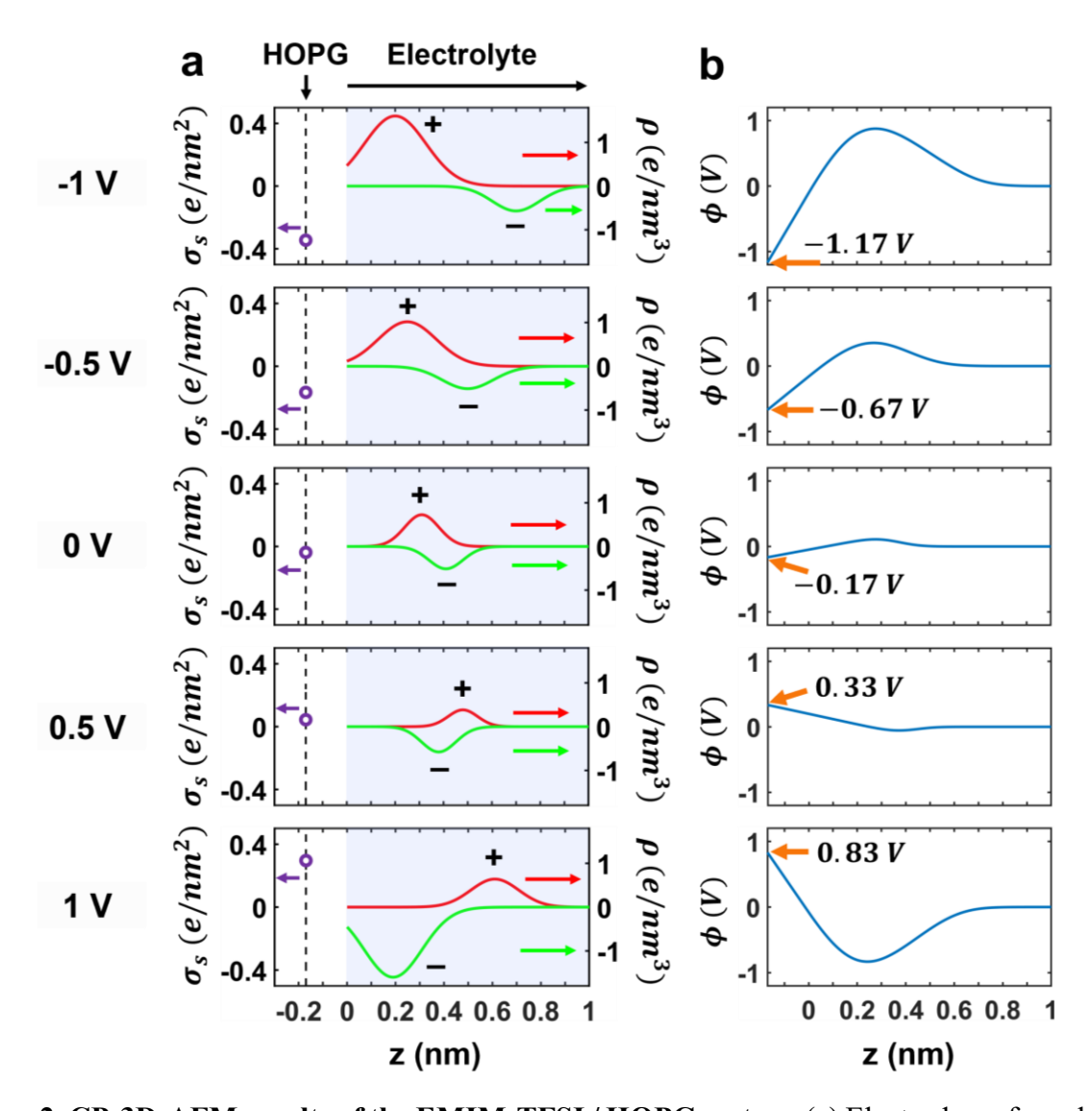


Figure 2. CP-3D-AFM results of the EMIM-TFSI / HOPG system. (a) Electrode surface charge density (σ_s) and EDL volumetric charge density (ρ) vs z at different electrode potentials (vs Pt). Red curves: positive charges; green: negative charges. (b) Corresponding electrostatic potential as a function of z; the potential values at the electrode surface (vs bulk electrolyte) are marked on the plots.

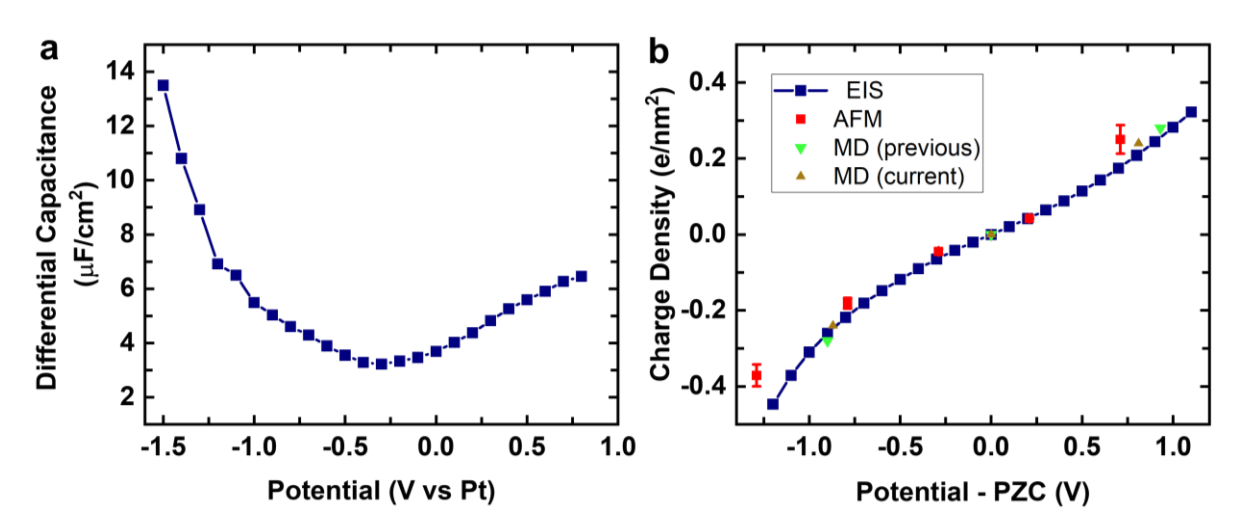


Figure 3. Quantification of the capacitive charging effects of EMIM-TFSI / HOPG. (a) Differential capacitance obtained from EIS measurements and equivalent circuit analysis. (b) Electrode surface charge density as a function of electrode potential (vs PZC), obtained from EIS, CP-3D-AFM, and MD simulations. Green inverted triangle: MD data from previous work³⁴; brown triangle: data from additional MD simulations in this work.

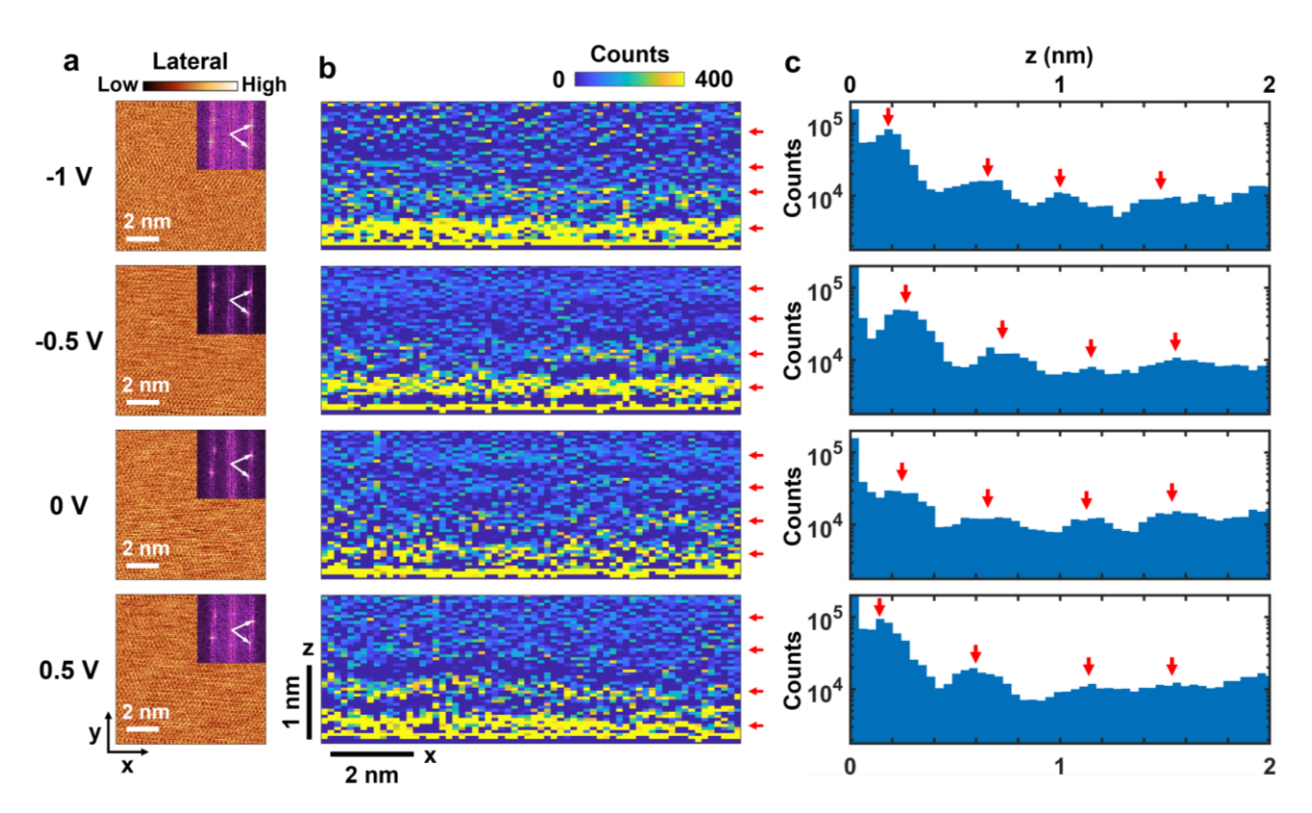


Figure 4. EC-3D-AFM results of 21 m LiTFSI in water / HOPG. (a) Lattice resolution images at different potentials (vs Pt), with the fast Fourier transform (FFT) images (14.5 nm⁻¹ × 14.5 nm⁻¹) shown as insets. White arrows on the FFT images mark the reciprocal lattice directions. (b) x-z count maps (background-subtracted) at various electrode potentials. (c) Corresponding count histograms as a function of z. The positions of the EDL layers are marked by red arrows in both the x-z maps and the z histograms.

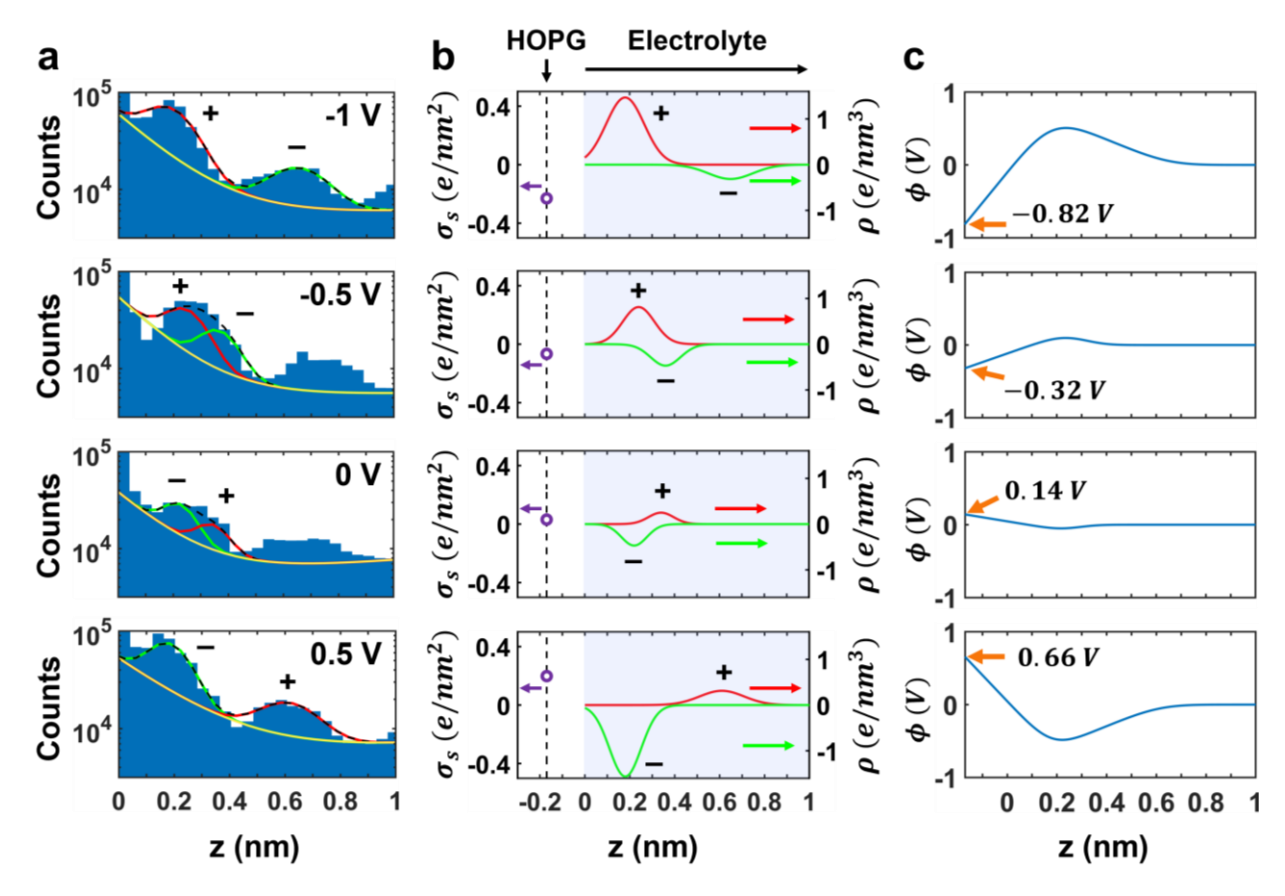


Figure 5. CP-3D-AFM analysis of 21 m LiTFSI in water / **HOPG.** (a) Charge peak fitting of the z count histograms. Yellow curves: background; red: positive charges; green: negative charges. (b) The extracted charge density profiles including the electrode surface and EDL. (c) Electrostatic potential profiles, with values of electrode surface potential marked.

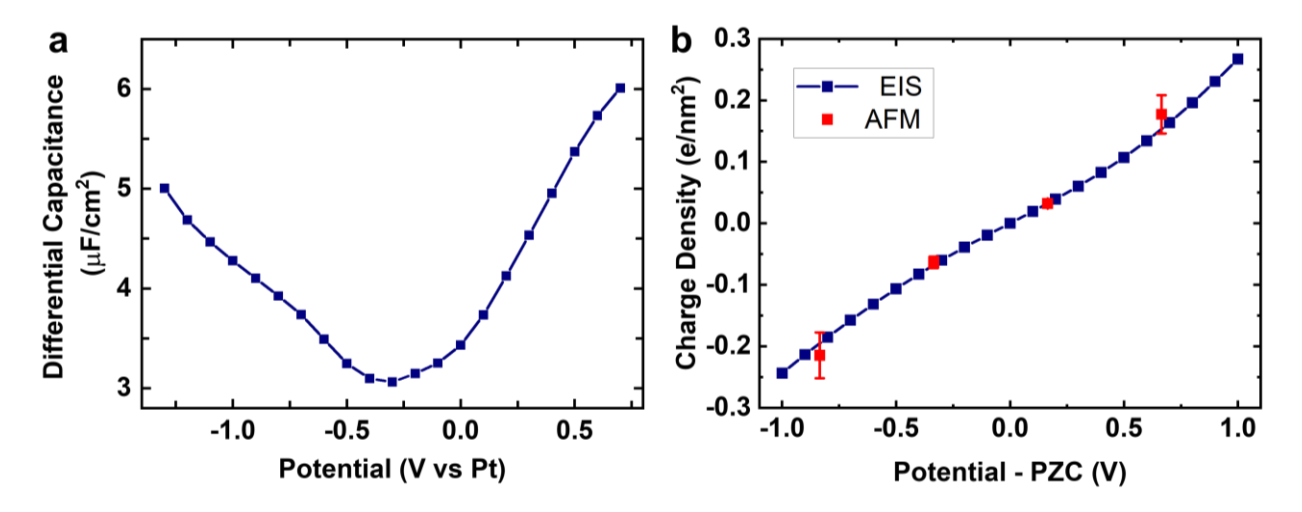


Figure 6. Quantification of the capacitive charging effects of 21 m LiTFSI in water / HOPG. (a) Differential capacitance obtained from EIS measurements and analysis. (b) Electrode surface charge density extracted from EIS and CP-3D-AFM.

Associated Content

Supporting Information

The Supporting Information is available free of charge online.

Supporting Notes S1, S2: Analysis methods for CP-3D-AFM and EIS.

Supporting Figures S1-S12: CP-3D-AFM analysis using additional charge peaks; examples showing the peak fitting procedures for CP-3D-AFM of EMIM-TFSI / HOPG; EIS spectra and equivalent circuit fitting; individual count histograms for charge density extraction, averaging and error analysis of EMIM-TFSI / HOPG; charge density comparison of EMIM-TFSI / HOPG between MD and CP-3D-AFM results; comparison of electrostatic potential profiles of EMIM-TFSI / HOPG between MD and CP-3D-AFM results; CV of WiS / HOPG; comparison of EC-3D-AFM count histograms of EMIM-TFSI / HOPG vs WiS / HOPG; count histograms of WiS/HOPG obtained from 3D-AFM imaging using two separate probes; detailed peak fitting processes for CP-3D-AFM analysis of WiS / HOPG; comparison of the differential capacitance profiles of EMIM-TFSI / HOPG vs WiS / HOPG; individual count histograms for charge density extraction, averaging and error analysis of WiS / HOPG.

Supporting Tables S1-S4: Fitting parameters corresponding to the CP-3D-AFM analysis procedures of EMIM-TFSI / HOPG and WiS / HOPG; AFM probe parameters; 3D-AFM imaging parameters.

Notes

The authors declare no competing interests.

Acknowledgements

L.K.S.B., K.S.P., S.Z. and Y.Z. acknowledge support from the National Science Foundation under Grant # 2137147. H.W. and N.R.A. acknowledge support from the National Science Foundation under Grant # 2137157. The experiments were performed in part in the Carl R. Woese Institute for Genomic Biology and in the Materials Research Laboratory at the University of Illinois.

References

- (1) Zhang, L. L.; Zhao, X. S. Carbon-Based Materials as Supercapacitor Electrodes. *Chem. Soc. Rev.* **2009**, *38*, 2520–2531.
- (2) Xu, K. Electrolytes and Interphases in Li-Ion Batteries and Beyond. *Chem. Rev.* **2014**, *114*, 11503–11618.
- von Wald Cresce, A.; Borodin, O.; Xu, K. Correlating Li⁺ Solvation Sheath Structure with Interphasial Chemistry on Graphite. *J. Phys. Chem. C* **2012**, *116*, 26111–26117.
- (4) Liu, T.; Lin, L.; Bi, X.; Tian, L.; Yang, K.; Liu, J.; Li, M.; Chen, Z.; Lu, J.; Amine, K.; et al. In Situ Quantification of Interphasial Chemistry in Li-Ion Battery. *Nat. Nanotechnol.* **2019**, *14*, 50–56.
- (5) Jiang, L.-L.; Yan, C.; Yao, Y.-X.; Cai, W.; Huang, J.-Q.; Zhang, Q. Inhibiting Solvent Co-Intercalation in a Graphite Anode by a Localized High-Concentration Electrolyte in Fast-Charging Batteries. *Angew. Chemie Int. Ed.* **2021**, *60*, 3402–3406.
- (6) Rosen, B. A.; Salehi-Khojin, A.; Thorson, M. R.; Zhu, W.; Whipple, D. T.; Kenis, P. J. A.; Masel, R. I. Ionic Liquid–Mediated Selective Conversion of CO₂ to CO at Low Overpotentials. *Science* **2011**, *334*, 643–644.
- (7) Strmcnik, D.; Kodama, K.; Van Der Vliet, D.; Greeley, J.; Stamenkovic, V. R.; Marković, N. M. The Role of Non-Covalent Interactions in Electrocatalytic Fuel-Cell Reactions on Platinum. *Nat. Chem.* **2009**, *1*, 466–472.
- (8) Liu, E.; Li, J.; Jiao, L.; Doan, H. T. T.; Liu, Z.; Zhao, Z.; Huang, Y.; Abraham, K. M.; Mukerjee, S.; Jia, Q. Unifying the Hydrogen Evolution and Oxidation Reactions Kinetics in Base by Identifying the Catalytic Roles of Hydroxyl-Water-Cation Adducts. *J. Am. Chem. Soc.* **2019**, *141*, 3232–3239.
- (9) Wang, A.; Li, J.; Zhang, T. Heterogeneous Single-Atom Catalysis. *Nat. Rev. Chem.* **2018**, 2, 65–81.
- (10) Hammes-Schiffer, S.; Galli, G. Integration of Theory and Experiment in the Modelling of Heterogeneous Electrocatalysis. *Nat. Energy* **2021**, *6*, 700–705.
- (11) Velasco-Velez, J.-J.; Wu, C. H.; Pascal, T. A.; Wan, L. F.; Guo, J.; Prendergast, D.; Salmeron, M. The Structure of Interfacial Water on Gold Electrodes Studied by X-Ray Absorption Spectroscopy. *Science* **2014**, *346*, 831–834.

- (12) Li, J.; Li, X.; Gunathunge, C. M.; Waegele, M. M. Hydrogen Bonding Steers the Product Selectivity of Electrocatalytic CO Reduction. *Proc. Natl. Acad. Sci.* **2019**, *116*, 9220–9229.
- (13) Montenegro, A.; Dutta, C.; Mammetkuliev, M.; Shi, H.; Hou, B.; Bhattacharyya, D.; Zhao, B.; Cronin, S. B.; Benderskii, A. V. Asymmetric Response of Interfacial Water to Applied Electric Fields. *Nature* **2021**, *594*, 62–65.
- (14) Wang, Y.-H.; Zheng, S.; Yang, W.-M.; Zhou, R.-Y.; He, Q.-F.; Radjenovic, P.; Dong, J.-C.; Li, S.; Zheng, J.; Yang, Z.-L.; et al. In Situ Raman Spectroscopy Reveals the Structure and Dissociation of Interfacial Water. *Nature* **2021**, *600*, 81–85.
- (15) Park, J.; Elmlund, H.; Ercius, P.; Yuk, J. M.; Limmer, D. T.; Chen, Q.; Kim, K.; Han, S. H.; Weitz, D. A.; Zettl, A.; et al. 3D Structure of Individual Nanocrystals in Solution by Electron Microscopy. *Science* **2015**, *349*, 290–295.
- (16) Wang, H.; Wu, C. H.; Eren, B.; Hao, Y.; Feng, B.; Fang, H.-T.; Salmeron, M. Operando STM Study of the Interaction of Imidazolium-Based Ionic Liquid with Graphite. *Energy Storage Mater.* **2019**, *20*, 139–145.
- (17) Kumeda, T.; Tajiri, H.; Sakata, O.; Hoshi, N.; Nakamura, M. Effect of Hydrophobic Cations on the Oxygen Reduction Reaction on Single–crystal Platinum Electrodes. *Nat. Commun.* 2018, 9, 4378.
- (18) Kondo, T.; Masuda, T.; Aoki, N.; Uosaki, K. Potential-Dependent Structures and Potential-Induced Structure Changes at Pt(111) Single-Crystal Electrode/Sulfuric and Perchloric Acid Interfaces in the Potential Region between Hydrogen Underpotential Deposition and Surface Oxide Formation by In Situ Su. *J. Phys. Chem. C* **2016**, *120*, 16118–16131.
- (19) Rakov, D. A.; Chen, F.; Ferdousi, S. A.; Li, H.; Pathirana, T.; Simonov, A. N.; Howlett, P. C.; Atkin, R.; Forsyth, M. Engineering High-Energy-Density Sodium Battery Anodes for Improved Cycling with Superconcentrated Ionic-Liquid Electrolytes. *Nat. Mater.* 2020, 19, 1096–1101.
- (20) Mao, X.; Brown, P.; Červinka, C.; Hazell, G.; Li, H.; Ren, Y.; Chen, D.; Atkin, R.; Eastoe, J.; Grillo, I.; et al. Self-Assembled Nanostructures in Ionic Liquids Facilitate Charge Storage at Electrified Interfaces. *Nat. Mater.* 2019, 18, 1350–1357.
- (21) Umeda, K.; Kobayashi, K.; Minato, T.; Yamada, H. Atomic-Level Viscosity Distribution in the Hydration Layer. *Phys. Rev. Lett.* **2019**, *122*, 116001.
- (22) Martin-Jimenez, D.; Chacon, E.; Tarazona, P.; Garcia, R. Atomically Resolved Three-Dimensional Structures of Electrolyte Aqueous Solutions near a Solid Surface. *Nat. Commun.* **2016**, *7*, 12164.
- (23) Martin-Jimenez, D.; Garcia, R. Identification of Single Adsorbed Cations on Mica–Liquid Interfaces by 3D Force Microscopy. *J. Phys. Chem. Lett.* **2017**, *8*, 5707–5711.
- Uhlig, M. R.; Martin-Jimenez, D.; Garcia, R. Atomic-Scale Mapping of Hydrophobic Layers on Graphene and Few-Layer MoS₂ and WSe₂ in Water. *Nat. Commun.* **2019**, *10*, 2606.
- (25) Benaglia, S.; Uhlig, M. R.; Hernández-Muñoz, J.; Chacón, E.; Tarazona, P.; Garcia, R. Tip

- Charge Dependence of Three-Dimensional AFM Mapping of Concentrated Ionic Solutions. *Phys. Rev. Lett.* **2021**, *127*, 196101.
- (26) Black, J. M.; Walters, D.; Labuda, A.; Feng, G.; Hillesheim, P. C.; Dai, S.; Cummings, P. T.; Kalinin, S. V; Proksch, R.; Balke, N. Bias-Dependent Molecular-Level Structure of Electrical Double Layer in Ionic Liquid on Graphite. *Nano Lett.* **2013**, *13*, 5954–5960.
- (27) Hayes, R.; Borisenko, N.; Tam, M. K.; Howlett, P. C.; Endres, F.; Atkin, R. Double Layer Structure of Ionic Liquids at the Au(111) Electrode Interface: An Atomic Force Microscopy Investigation. *J. Phys. Chem. C* **2011**, *115*, 6855–6863.
- (28) Segura, J. J.; Elbourne, A.; Wanless, E. J.; Warr, G. G.; Voïtchovsky, K.; Atkin, R. Adsorbed and near Surface Structure of Ionic Liquids at a Solid Interface. *Phys. Chem. Chem. Phys.* **2013**, *15*, 3320–3328.
- (29) Jurado, L. A.; Espinosa-Marzal, R. M. Insight into the Electrical Double Layer of an Ionic Liquid on Graphene. *Sci. Rep.* **2017**, *7*, 4225.
- (30) Sheehan, A.; Jurado, L. A.; Ramakrishna, S. N.; Arcifa, A.; Rossi, A.; Spencer, N. D.; Espinosa-Marzal, R. M. Layering of Ionic Liquids on Rough Surfaces. *Nanoscale* **2016**, *8*, 4094–4106.
- (31) Hayes, R.; El Abedin, S. Z.; Atkin, R. Pronounced Structure in Confined Aprotic Room-Temperature Ionic Liquids. *J. Phys. Chem. B* **2009**, *113*, 7049–7052.
- (32) Umeda, K.; Zivanovic, L.; Kobayashi, K.; Ritala, J.; Kominami, H.; Spijker, P.; Foster, A. S.; Yamada, H. Atomic-Resolution Three-Dimensional Hydration Structures on a Heterogeneously Charged Surface. *Nat. Commun.* **2017**, *8*, 2111.
- (33) Umeda, K.; Kobayashi, K.; Minato, T.; Yamada, H. Atomic-Scale 3D Local Hydration Structures Influenced by Water-Restricting Dimensions. *Langmuir* **2018**, *34*, 9114–9121.
- (34) Zhou, S.; Panse, K. S.; Motevaselian, M. H.; Aluru, N. R.; Zhang, Y. Three-Dimensional Molecular Mapping of Ionic Liquids at Electrified Interfaces. *ACS Nano* **2020**, *14*, 17515–17523.
- (35) Panse, K. S.; Wu, H.; Zhou, S.; Zhao, F.; Aluru, N. R.; Zhang, Y. Innermost Ion Association Configuration Is a Key Structural Descriptor of Ionic Liquids at Electrified Interfaces. *J. Phys. Chem. Lett.* **2022**, *13*, 9464–9472.
- (36) Collins, L.; Kilpatrick, J. I.; Kalinin, S. V; Rodriguez, B. J. Towards Nanoscale Electrical Measurements in Liquid by Advanced KPFM Techniques: A Review. *Reports Prog. Phys.* **2018**, *81*, 86101.
- (37) Favaro, M.; Jeong, B.; Ross, P. N.; Yano, J.; Hussain, Z.; Liu, Z.; Crumlin, E. J. Unravelling the Electrochemical Double Layer by Direct Probing of the Solid/Liquid Interface. *Nat. Commun.* **2016**, *7*, 12695.
- (38) Kobayashi, N.; Asakawa, H.; Fukuma, T. Dual Frequency Open-Loop Electric Potential Microscopy for Local Potential Measurements in Electrolyte Solution with High Ionic Strength. *Rev. Sci. Instrum.* **2012**, *83*, 33709.

- (39) Kobayashi, N.; Asakawa, H.; Fukuma, T. Nanoscale Potential Measurements in Liquid by Frequency Modulation Atomic Force Microscopy. *Rev. Sci. Instrum.* **2010**, *81*, 123705.
- (40) Hirata, K.; Kitagawa, T.; Miyazawa, K.; Okamoto, T.; Fukunaga, A.; Takatoh, C.; Fukuma, T. Visualizing Charges Accumulated in an Electric Double Layer by Three-Dimensional Open-Loop Electric Potential Microscopy. *Nanoscale* **2018**, *10*, 14736–14746.
- (41) Ishisone, K.; Ori, G.; Boero, M. Structural, Dynamical, and Electronic Properties of the Ionic Liquid 1-Ethyl-3-Methylimidazolium Bis(Trifluoromethylsulfonyl)Imide. *Phys. Chem. Chem. Phys.* **2022**, *24*, 9597–9607.
- (42) McEldrew, M.; Goodwin, Z. A. H.; Kornyshev, A. A.; Bazant, M. Z. Theory of the Double Layer in Water-in-Salt Electrolytes. *J. Phys. Chem. Lett.* **2018**, *9*, 5840–5846.
- (43) Flores, E.; Åvall, G.; Jeschke, S.; Johansson, P. Solvation Structure in Dilute to Highly Concentrated Electrolytes for Lithium-Ion and Sodium-Ion Batteries. *Electrochim. Acta* **2017**, *233*, 134–141.
- (44) Mena, S.; Ribas, E.; Richart, C.; Gallardo, I.; Faraudo, J.; Shaw, S. K.; Guirado, G. Electrochemical Tools to Disclose the Electrochemical Reduction Mechanism of CO₂ in Aprotic Solvents and Ionic Liquids. *J. Electroanal. Chem.* **2021**, 895, 115411.
- (45) Wang, X.; Salari, M.; Jiang, D.; Chapman Varela, J.; Anasori, B.; Wesolowski, D. J.; Dai, S.; Grinstaff, M. W.; Gogotsi, Y. Electrode Material-Ionic Liquid Coupling for Electrochemical Energy Storage. *Nat. Rev. Mater.* 2020, 5, 787–808.
- (46) Bazant, M. Z.; Storey, B. D.; Kornyshev, A. A. Double Layer in Ionic Liquids: Overscreening versus Crowding. *Phys. Rev. Lett.* **2011**, *106*, 46102.
- (47) Vatamanu, J.; Borodin, O.; Smith, G. D. Molecular Dynamics Simulations of Atomically Flat and Nanoporous Electrodes with a Molten Salt Electrolyte. *Phys. Chem. Chem. Phys.* **2010**, *12*, 170–182.
- (48) Hu, Z.; Vatamanu, J.; Borodin, O.; Bedrov, D. A Molecular Dynamics Simulation Study of the Electric Double Layer and Capacitance of [BMIM][PF6] and [BMIM][BF4] Room Temperature Ionic Liquids near Charged Surfaces. *Phys. Chem. Chem. Phys.* **2013**, *15*, 14234–14247.
- (49) Klein, J. M.; Panichi, E.; Gurkan, B. Potential Dependent Capacitance of [EMIM][TFSI], [N₁₁₁₄][TFSI] and [PYR₁₃][TFSI] Ionic Liquids on Glassy Carbon. *Phys. Chem. Chem. Phys.* **2019**, *21*, 3712–3720.
- (50) Gu, C.; Yin, L.; Li, S.; Zhang, B.; Liu, X.; Yan, T. Differential Capacitance of Ionic Liquid and Mixture with Organic Solvent. *Electrochim. Acta* **2021**, *367*, 137517.
- (51) Bozym, D. J.; Uralcan, B.; Limmer, D. T.; Pope, M. A.; Szamreta, N. J.; Debenedetti, P. G.; Aksay, I. A. Anomalous Capacitance Maximum of the Glassy Carbon–Ionic Liquid Interface through Dilution with Organic Solvents. *J. Phys. Chem. Lett.* **2015**, *6*, 2644–2648.
- (52) Vatamanu, J.; Borodin, O.; Bedrov, D.; Smith, G. D. Molecular Dynamics Simulation Study of the Interfacial Structure and Differential Capacitance of Alkylimidazolium Bis(Trifluoromethanesulfonyl)Imide [Cnmim][TFSI] Ionic Liquids at Graphite Electrodes.

- J. Phys. Chem. C 2012, 116, 7940-7951.
- (53) Sambasivarao, S. V; Acevedo, O. Development of OPLS-AA Force Field Parameters for 68 Unique Ionic Liquids. *J. Chem. Theory Comput.* **2009**, *5*, 1038–1050.
- (54) Doherty, B.; Zhong, X.; Gathiaka, S.; Li, B.; Acevedo, O. Revisiting OPLS Force Field Parameters for Ionic Liquid Simulations. *J. Chem. Theory Comput.* **2017**, *13*, 6131–6145.
- (55) Suo, L.; Borodin, O.; Gao, T.; Olguin, M.; Ho, J.; Fan, X.; Luo, C.; Wang, C.; Xu, K. "Water-in-Salt" Electrolyte Enables High-Voltage Aqueous Lithium-Ion Chemistries. *Science* **2015**, *350*, 938–943.
- (56) Jaumaux, P.; Yang, X.; Zhang, B.; Safaei, J.; Tang, X.; Zhou, D.; Wang, C.; Wang, G. Localized Water-In-Salt Electrolyte for Aqueous Lithium-Ion Batteries. *Angew. Chemie Int. Ed.* **2021**, *60*, 19965–19973.
- (57) Wu, X.; Xu, Y.; Zhang, C.; Leonard, D. P.; Markir, A.; Lu, J.; Ji, X. Reverse Dual-Ion Battery via a ZnCl₂ Water-in-Salt Electrolyte. *J. Am. Chem. Soc.* **2019**, *141*, 6338–6344.
- (58) Suo, L.; Borodin, O.; Wang, Y.; Rong, X.; Sun, W.; Fan, X.; Xu, S.; Schroeder, M. A.; Cresce, A. V; Wang, F.; et al. "Water-in-Salt" Electrolyte Makes Aqueous Sodium-Ion Battery Safe, Green, and Long-Lasting. *Adv. Energy Mater.* **2017**, *7*, 1701189.
- (59) Lukatskaya, M. R.; Feldblyum, J. I.; Mackanic, D. G.; Lissel, F.; Michels, D. L.; Cui, Y.; Bao, Z. Concentrated Mixed Cation Acetate "Water-in-Salt" Solutions as Green and Low-Cost High Voltage Electrolytes for Aqueous Batteries. *Energy Environ. Sci.* 2018, 11, 2876–2883.
- (60) Li, Z.; Jeanmairet, G.; Méndez-Morales, T.; Rotenberg, B.; Salanne, M. Capacitive Performance of Water-in-Salt Electrolytes in Supercapacitors: A Simulation Study. J. Phys. Chem. C 2018, 122, 23917–23924.
- (61) Zhang, R.; Han, M.; Ta, K.; Madsen, K. E.; Chen, X.; Zhang, X.; Espinosa-Marzal, R. M.; Gewirth, A. A. Potential-Dependent Layering in the Electrochemical Double Layer of Water-in-Salt Electrolytes. ACS Appl. Energy Mater. 2020, 3, 8086–8094.
- (62) Han, M.; Zhang, R.; Gewirth, A. A.; Espinosa-Marzal, R. M. Nanoheterogeneity of LiTFSI Solutions Transitions Close to a Surface and with Concentration. *Nano Lett.* **2021**, *21*, 2304–2309.
- (63) Sillars, F. B.; Fletcher, S. I.; Mirzaeian, M.; Hall, P. J. Variation of Electrochemical Capacitor Performance with Room Temperature Ionic Liquid Electrolyte Viscosity and Ion Size. *Phys. Chem. Chem. Phys.* **2012**, *14*, 6094–6100.
- (64) Elbourne, A.; McDonald, S.; Voïchovsky, K.; Endres, F.; Warr, G. G.; Atkin, R. Nanostructure of the Ionic Liquid–Graphite Stern Layer. *ACS Nano* **2015**, *9*, 7608–7620.
- (65) Black, J. M.; Zhu, M.; Zhang, P.; Unocic, R. R.; Guo, D.; Okatan, M. B.; Dai, S.; Cummings, P. T.; Kalinin, S. V; Feng, G.; et al. Fundamental Aspects of Electric Double Layer Force-Distance Measurements at Liquid-Solid Interfaces Using Atomic Force Microscopy. *Sci. Rep.* 2016, 6, 32389.

- (66) Nightingale, E. R. Phenomenological Theory of Ion Solvation. Effective Radii of Hydrated Ions. *J. Phys. Chem.* **1959**, *63*, 1381–1387.
- (67) Rempe, S. B.; Pratt, L. R.; Hummer, G.; Kress, J. D.; Martin, R. L.; Redondo, A. The Hydration Number of Li⁺ in Liquid Water. *J. Am. Chem. Soc.* **2000**, *122*, 966–967.
- (68) Kim, J.; Zhao, F.; Zhou, S.; Panse, K. S.; Zhang, Y. Spectroscopic Investigation of the Structure of a Pyrrolidinium-Based Ionic Liquid at Electrified Interfaces. *J. Chem. Phys.* **2022**, *156*, 114701.
- (69) Bard, A. J.; Faulkner, L. R. *Electrochemical Methods: Fundamentals and Applications*, 2nd ed.; Wiley: New York, 2001.